

Machine Learning Approach to Force Reconstruction in Photoelastic Materials

Renat Sergazinov

Department of Statistics, Texas A&M University, Blocker Building, 3143, 155 Ireland St, College Station, TX 77843, USA

E-mail: mrsergazinov@tamu.edu

Miroslav Kramár

Department of Mathematics, University of Oklahoma, 601 Elm Avenue, Norman, OK 73019, USA

E-mail: miro@ou.edu

Abstract. Photoelastic techniques have a long tradition in both qualitative and quantitative analysis of the stresses in granular materials. Over the last two decades, computational methods for reconstructing forces between particles from their photoelastic response have been developed by many different experimental teams. Unfortunately, all of these methods are computationally expensive. This limits their use for processing extensive data sets that capture the time evolution of granular ensembles consisting of a large number of particles. In this paper, we present a novel approach to this problem which leverages the power of convolutional neural networks to recognize complex spatial patterns. The main drawback of using neural networks is that training them usually requires a large labeled data set which is hard to obtain experimentally. We show that this problem can be successfully circumvented by pretraining the networks on a large synthetic data set and then fine-tuning them on much smaller experimental data sets. Due to our current lack of experimental data, we demonstrate the potential of our method by changing the size of the considered particles which alters the exhibited photoelastic patterns more than typical experimental errors.

1. Introduction

Granular materials consist of macroscopic particles, they are ubiquitous in nature and indispensable for a large variety of human activities. Powders and grains play a crucial role in many applications such as agriculture, construction, and chemical industry. As noted in [1], the worldwide annual production of grains and aggregates of various kinds exceeds ten billion metric tons. Moreover, granular materials are the second most manipulated materials in the industry after water. So, understanding the physics of granular materials has a major economic impact.

Despite extensive efforts by scientists, properties of granular systems are still not well understood and some of them remain rather obscure. However, it is well

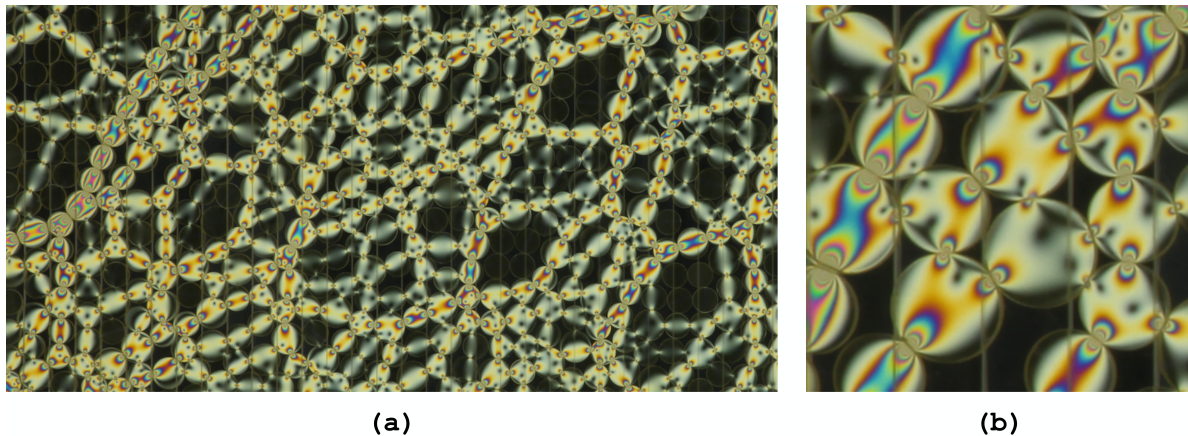


Figure 1. [Courtesy of D. Wang.] (a) An example of a photoelastic response of particles in a sheared system [13] shows that the stresses (forces) in the material propagate along bright filamentary structures called force chains. (b) Detail of the photoelastic pattern on individual particles. Similar patterns are produced by using monochromatic light and they can be used to reconstruct forces acting between the particles.

known that the forces in these systems do not propagate uniformly [2, 3, 4] but along highly anisotropic filamentary structures called force chains, shown in Fig. 1. The structure of the force chains is crucial for revealing the underlying physical causes of a wide variety of phenomena [5, 6, 7, 8, 9] and plays an important role in determining the mechanical properties of granular systems. The first attempts to experimentally study stresses in granular systems by using photoelastic materials were conducted by Wakabayashi [10] and Dantu [11]. Later, Behringer and Majmudar used photoelastic methods [3] to estimate the forces acting between the particles. We refer the reader to [12] for a comprehensive review of photoelastic methods and their applications to granular materials.

The visualization of the force chains, depicted in Fig. 1(a), is produced by placing an ensemble of photoelastic particles between two polarizing filters. The fact that the degree of birefringence at each location in the photoelastic material depends on local stress produces a visual pattern of alternating bright and dark fringes, visible in Fig. 1(b). The precise pattern depends in a complex manner on the orientation of the polarizers, the shape of the material, and how it is stressed. If a circular particle is illuminated by monochromatic light, then its photoelastic response can be computed from the forces acting on it, see Section 2 for more details. However, to determine the forces from the pattern one needs to solve a much more complicated inverse problem.

Several computational methods for reconstructing the forces between circular particles were implemented by different groups [14, 15]. While the implementations differ, the algorithms are based on the general ideas presented in [3] and they roughly proceed as follows. First, the positions of the particles are calculated and the force bearing contacts between them are identified. Then, for each particle the forces acting

on it at the force bearing contacts are guessed. Finally, an optimization algorithm is used to minimize the difference between the experimentally observed pattern exhibited by the particle and the pattern generated from the reconstructed forces.

As mentioned in [12], the positions of the particles can be identified with high accuracy using the Hough transform. However, there might be large discrepancies when it comes to force reconstruction. The reconstructed force between two particles can considerably vary depending on which of the two particles is used for the reconstruction. Moreover, a computationally expensive evaluation of the photoelastic response has to be performed in every iteration of the optimization process. In this paper, we use machine learning to accurately reconstruct forces acting on a particle from its photoelastic response.

Machine learning algorithms are very efficient for finding and recognizing patterns in complex data [16, 17]. They are extensively used in speech and image recognition as well as predictive analysis, search systems, data visualization, and anomaly detection [17, 18, 19, 20]. In particular, convolutional neural networks (CNN) are well suited for the recognition of spatial patterns [17, 21, 22] such as those exhibited by the photoelastic particles.

In this paper, we show that CNNs produce accurate force reconstruction on synthetic data even if the patterns are corrupted by noise. This is visually demonstrated by Fig. 2. The patterns depicted in the top row are computer-generated photoelastic responses of a single particle to a variety of different (known) forces acting on it. The images in the middle row are created by adding Gaussian noise to the patterns and serve as an input for the CNN. Finally, the bottom row shows the patterns generated from the reconstructed forces. Note that the corresponding images in the top and bottom row are quite similar. While the precise results are presented in Section 6, we just mention that the mean absolute error in predicted positions of the force impact points is smaller than 1.25 pixels and the mean relative error of the predicted force magnitudes is approximately 4%.

To achieve high accuracy of the force reconstruction we experimented with diverse architectures of CNNs. In particular, we considered two different strategies: 1) building a custom model, and 2) using transfer learning [23, 24, 25, 26]. Currently, there are no rigorous methods for choosing a proper architecture for a custom model. Thus, our extensive experiments were guided by heuristic methods based on balancing the trade-off between bias and variance of the model [27, 28]. We also utilized transfer learning to circumvent this tedious process. Namely, we retrained the VGG16 model [22] that provides an outstanding classification of real-world images to perform our task. However, the accuracy achieved in this way is lower than the accuracy of our custom model. We believe that this is caused by negative transfer phenomena, due to dissimilarities between the original and new task [23, 29], as well as a good choice of the architecture of our custom model.

Despite the high accuracy of our custom model trained on synthetic data, we cannot guarantee that its predictions on the experimental data would be equally accurate.

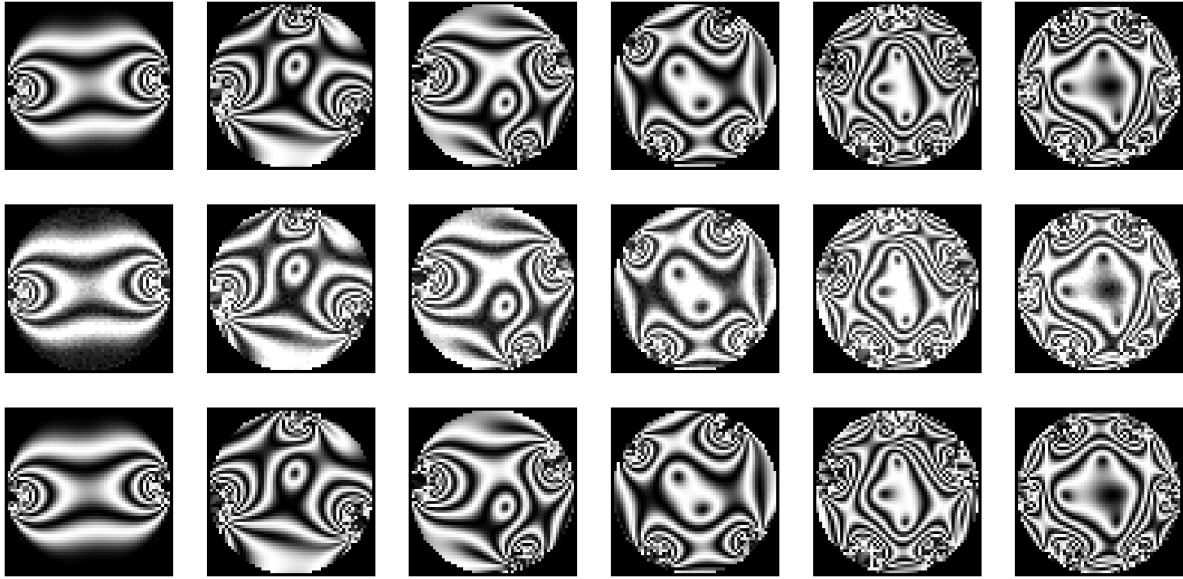


Figure 2. Top row: Computer generated photoelastic responses on a single particle for a variety of different forces. Middle row: The patterns produced from the images in the top row by adding Gaussian noise. Bottom row: Computer generated photoelastic response based on the forces reconstructed by a CNN from the noised particle images depicted in the middle row.

Unfortunately, training the models directly on experimental data is rather unrealistic because the required number of labeled samples is too large to produce experimentally. To overcome this problem we suggest to pretrain the model on synthetic data and then transfer it to the experimental data by using a relatively small data set. The danger of negative transfer phenomena is mitigated by similarities between two data sets. These methods were already successfully used for different tasks such as object detection, optical flow estimation, and scene understanding [30, 31, 32]. Currently, we do not have the necessary experimental data to prove our claim. Thus, we demonstrate the potential of this approach by transferring our pretrained model to smaller-sized particles, which serve as a proxy for the worst-case difference between experimental and synthetic data.

The paper is organized as follows. Section 2 contains a brief overview of photoelastic theory and explains how the photoelastic response on a circular particle is computed from the forces acting on it. In Section 3 we formalize the problem of force reconstruction and summarize earlier works concerned with solving this problem. The machine learning framework for the force reconstruction is discussed in Section 4 and the CNN models defined there are trained using the protocol outlined in Section 5. Finally, our results are presented in Section 6. We conclude the paper with some final remarks in Section 7.

2. Photoelastic Theory

Photoelastic methods are widely used for quantitative analysis of stress in granular media. In this section, we provide a brief overview of photoelasticity while a detailed

treatment can be found in [33]. A comprehensive review of the experimental methods for granular media based on photoelastic theory is presented in [12]. Figure 2 shows a pattern of dark and bright fringes formed by illuminating photoelastic particles placed in between two polarizing filters. The intensity field $I(x, y)$ of the pattern depends on local stresses inside the particle. To be more precise, let us consider the stress tensor inside the particle

$$\sigma(x, y) = \begin{pmatrix} \sigma_{xx}(x, y) & \sigma_{xy}(x, y) \\ \sigma_{xy}(x, y) & \sigma_{yy}(x, y) \end{pmatrix}.$$

We denote its eigenvalues (principal stresses) by

$$\sigma_{\pm}(x, y) = \frac{1}{2} \left(\sigma_{xx}(x, y) + \sigma_{yy}(x, y) \pm \sqrt{(\sigma_{xx}(x, y) + \sigma_{yy}(x, y))^2 - 4\sigma_{xy}^2(x, y)} \right).$$

The intensity field exhibited by a particle is then given by

$$I(x, y) = I_0 \sin^2 \frac{\pi(\sigma_+(x, y) - \sigma_-(x, y))hC(\lambda)}{\lambda}, \quad (1)$$

where h is the material thickness, λ is the wavelength of light, C is the stress-optic coefficient dependent on λ , and I_0 is a normalization constant related to the intensity of the light. In this paper, we consider 8-bit grayscale digital images and set $I_0 = 255$. Without loss of generality we suppose that $hC(\lambda)/\lambda = 1$.

The stress tensor can be computed from the forces acting on the particle using elasticity theory [34, 35]. We briefly explain how the tensor is computed on a single particle while a detailed treatment in the case of three forces can be found in [36]. Due to the nature of the problem, we can suppose that the Saint-Venant's compatibility condition is satisfied, i.e., there are no gaps or overlaps in the material. In the absence of internal body forces, this condition can be formulated by the following equation

$$\frac{\partial^2 \epsilon_{xx}}{\partial y^2} - 2 \frac{\partial^2 \epsilon_{xy}}{\partial x \partial y} + \frac{\partial^2 \epsilon_{yy}}{\partial x^2} = 0, \quad (2)$$

where ϵ is the strain tensor. To write the above equation in terms of stress we use the generalized Hooke's law that imposes the following linear strain-stress relation:

$$\epsilon_{xx} = \frac{\sigma_{xx} - \nu \sigma_{yy}}{E}, \quad \epsilon_{yy} = \frac{\sigma_{yy} - \nu \sigma_{xx}}{E}, \quad \epsilon_{xy} = \frac{(1 + \nu) \sigma_{xy}}{E}, \quad (3)$$

where ν is the Poisson's ratio and E is the Young's modulus. The fact that the particle is in mechanical equilibrium implies

$$\begin{aligned} \frac{\partial \sigma_{xx}}{\partial x} + \frac{\partial \sigma_{xy}}{\partial y} &= 0, \\ \frac{\partial \sigma_{yy}}{\partial y} + \frac{\partial \sigma_{xy}}{\partial x} &= 0. \end{aligned} \quad (4)$$

To make sure that the stress tensor satisfies the equilibrium condition (4) we search for a solution in the form of the Airy stress function φ and express the components of the tensor σ as

$$\sigma_{xx} = \frac{\partial^2 \varphi}{\partial y^2}, \quad \sigma_{yy} = \frac{\partial^2 \varphi}{\partial x^2}, \quad \sigma_{xy} = \frac{\partial^2 \varphi}{\partial x \partial y}. \quad (5)$$

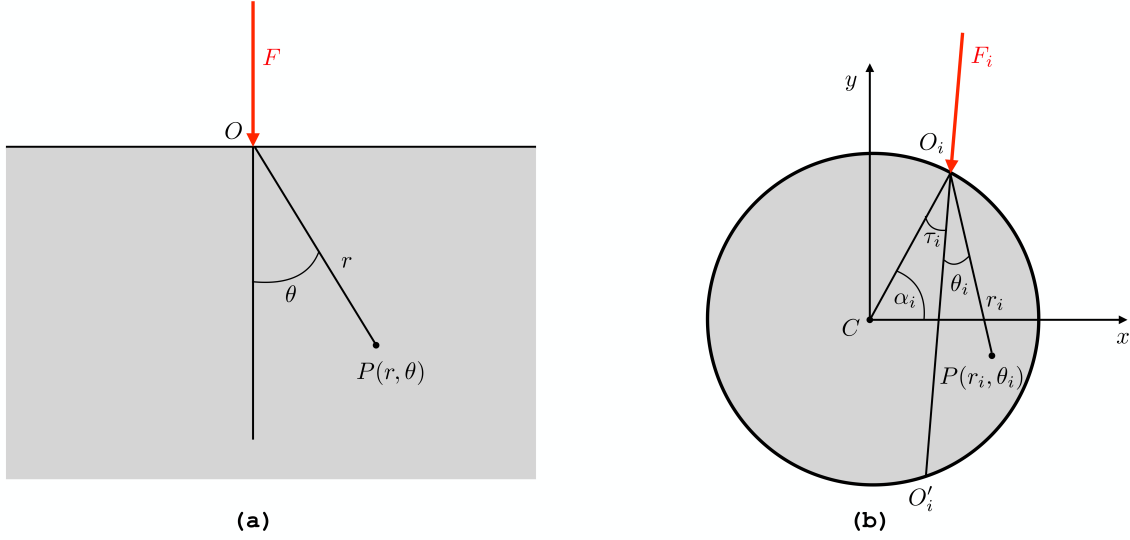


Figure 3. (a) A semi-infinite plane with a force acting on it at a single point O . To compute the stress at any point P it is convenient to use the polar coordinates based in the point O measuring the angle θ counterclockwise from the direction of the force. (b) Schematic representation of a particle. Only a single force $\{(F_i, \alpha_i, \tau_i)\}$ acting on this particle is depicted. The magnitude of this force is F_i . The position of the impact point O_i on the boundary of the disk is encoded by the angle α_i measured counterclockwise from the x -axis. The angle τ_i indicates how much the force deviates from pointing to the center of the particle. To compute the stress caused by this force we use the polar coordinates based at the point O_i measuring the angle θ_i counterclockwise from the direction of the force.

By combining Equations (3) and (5) we get an expression for the strain tensor in terms of φ . We substitute this expression into Equation (2) and obtain the final equation

$$\left(\frac{\partial^2}{\partial x^2} + \frac{\partial^2}{\partial y^2}\right) \left(\frac{\partial^2 \varphi}{\partial x^2} + \frac{\partial^2 \varphi}{\partial y^2}\right) = 0. \quad (6)$$

As is typical for partial differential equations we need to impose the correct boundary conditions. In our case, it is natural to require that there is no stress on the boundary of the particle except at the points where the external forces act on it.

To solve Equation (6) we exploit the fact that its solution is well known for a semi-infinite plane with a single perpendicular force acting on it at some point O , see Fig. 3(a). Let us consider a polar coordinate system based in O with angles measured counterclockwise from the force vector. In this coordinate system, the Airy stress function is given by $\varphi(r, \theta) = \frac{F}{\pi h} r \theta \sin \theta$, where F is the magnitude of the force and h is the thickness of the plane. In this coordinate system the stress tensor can be written as

$$\sigma_{rr}(r, \theta) = -\frac{2F}{\pi h} \frac{\cos \theta}{r}, \quad \sigma_{\theta\theta}(r, \theta) = 0, \quad \sigma_{r\theta}(r, \theta) = 0. \quad (7)$$

Now we turn our attention to an elastic disc exposed to M external forces. As indicated in Fig. 3(b), each of these forces can be encoded by a triplet (F_i, α_i, τ_i) . The

value F_i is the magnitude of the i -th force measured in Newtons. The impact point O_i of this force is determined by an angle α_i between the x -axis and the line connecting the center of the particle to O_i . Finally, τ_i is the angle between the direction of the force and the line segment $\overline{O_iC}$. The angles α_i and τ_i are measured counterclockwise in radians. The fact that Equation (6) is linear makes it possible to compute the final stress $\sigma(x, y)$ by summing up the stresses $\sigma^i(x, y)$ caused by individual forces.

Inspired by the example of the semi-infinite plane, we seek the solution for the stress due to the force (F_i, α_i, τ_i) in the polar coordinates (r_i, θ_i) centered at the point O_i measuring the angle θ_i counterclockwise from the direction of the force, see Fig. 3(b). In this coordinates the stress σ^i can be written as

$$\sigma_{r_i r_i}^i(r_i, \theta_i) = -\frac{2F_i \cos \theta_i}{\pi h} \frac{F_i}{r_i} + \frac{F_i}{\pi R h} \cos \tau_i, \quad \sigma_{\theta_i \theta_i}^i(r_i, \theta_i) = 0, \quad \sigma_{r_i \theta_i}^i(r_i, \theta_i) = 0, \quad (8)$$

where h is the thickness of the particle and R is its radius. The first term of $\sigma_{r_i r_i}^i(r_i, \theta_i)$ is analogous to the solution on the semi-infinite plane and the second term is added to ensure that the boundary condition (no stress except at the impact points) is satisfied. Note that each of the stress tensors σ^i is expressed in a different polar coordinate system. To obtain the full stress tensor $\sigma(x, y)$ in Cartesian coordinates we perform appropriate changes of coordinate systems as we sum up the individual stresses. So the total stress is

$$\sigma(x, y) = \sum_{i=1}^M T(\theta_i(x, y)) \sigma^i(r_i(x, y), \theta_i(x, y)), \quad (9)$$

where the matrix $T(\theta)$ rotates the plane by the angle θ .

3. Force Reconstruction from Photoelastic Response

In the previous section, we explained how to compute the photoelastic response of a circular particle if the forces acting on it are known. Extracting the forces acting on individual particles from experimental data is a much more complicated problem. Figure 1 is an example of an experimental image of the photoelastic patterns exhibited by an ensemble of particles. This image is only shown to illustrate the patterns and cannot be directly used for the force reconstruction which requires monochromatic lighting of the particles.

There are several computational packages [15, 14] that implement the force reconstruction based on the technique pioneered in [3]. As explained in [12], these methods require two images of the ensemble. The first image taken in unpolarized light is used to extract the positions of the particles and create a preliminary list of force bearing contacts between the particles. This list is then refined using the photoelastic patterns visible in the second image taken in polarized monochromatic light. The same image is also used to reconstruct forces on the individual particles. For each particle, an initial list of forces acting at the force bearing contacts is guessed based on a squared local gradient average of the pattern. Then, an optimization algorithm is used to minimize

the L_2 difference between the experimentally captured pattern exhibited by the particle and the pattern generated from the reconstructed forces.

As indicated in [12], the positions of the particles can be computed with high accuracy using the Hough transform. On the other hand, we are not aware of any systematic study of the accuracy of the force reconstruction. In particular, reconstruction of the force acting between two particles can considerably vary depending on which of the two particles is used for the reconstruction [12]. Therefore, we do not consider the problem of detecting the positions of the particles and only concentrate on force reconstruction from the photoelastic response of the individual particles.

In this paper, we reconstruct the forces $\{(F_i, \alpha_i, \theta_i)\}_{i=1}^M$ acting on a particle by exploiting the natural constraints due to geometry and physical properties of the particles typically used in experiments. We summarize these constraints in the rest of this section.

In principle, there could be a large number of forces acting on a single particle but this is not the case if the sizes of particles in the ensemble do not vary too much, see Figure 1. In this case, the number of forces acting on a particle is typically smaller than seven. If the system consists of monodisperse (same size) particles this upper bound is sharp. To avoid technicalities and demonstrate the ideas, we concentrate on monodisperse particles. By simple modifications indicated in Section 7, our method can be expanded to bidisperse as well as polydisperse materials. In the case of monodisperse particles the impact points at which the forces act on the particle cannot be too close to each other. To be more precise, the angles α_i encoding positions of the impact points have to satisfy

$$|\alpha_i - \alpha_j| \geq \frac{\pi}{3}, \text{ if } i \neq j. \quad (10)$$

The photoelastic theory presented in Section 2 is only valid if the particles are in mechanical equilibrium. Thus, to ensure that the reconstruction works properly, particles have to be allowed to equilibrate before collecting the data. The fact that the particles are in a mechanical equilibrium imposes force balance

$$\left(\sum_{i=1}^M F_i \cos \alpha_i, \sum_{i=1}^M F_i \sin \alpha_i \right) = (0, 0), \quad (11)$$

and torque balance

$$\sum_{i=1}^M F_i \sin \theta_i = 0 \quad (12)$$

constrains on each particle. Moreover, the force balance on a particle implies that $M \geq 2$.

Finally, the friction coefficient μ of the particles is typically smaller than 1 and so the angles τ_i satisfy

$$-\frac{\pi}{2} \leq \tau_i \leq \frac{\pi}{2}. \quad (13)$$

For example the friction coefficient of the particles shown in Fig. 1 is $\mu = 0.8$ as reported in [13]. This further reduces the possible range for τ_i .

4. Machine Learning Approach to Force Reconstruction

In this section, we set up a machine learning framework for reconstructing the forces acting on a particle from its photoelastic response. We will use convolutional neural networks (CNN) which are well suited for the recognition of spatial patterns in digital images [17, 21, 22]. The choice of a particular CNN model is rather challenging because there is no rigorous theory to design a neural network for a particular task. Heuristic methods are based on balancing the trade-off between bias and variance of the model. In particular, the model has to be sufficiently complex to represent the given problem otherwise its predictions will be poor. On the other hand, if the model is too complex, then it is likely to overfit the training data and decrease the generalization power of the model [27, 28]. Therefore, careful examination of the data and assessment of different models has to be conducted to choose a proper architecture. In this paper we experiment with two different strategies: 1) building a custom model, and 2) using transfer learning [23, 24, 25, 26].

The advantage of building a custom model from scratch is that it offers a lot of flexibility in terms of design. In principle, it allows us to tailor the most suitable model for the data. However, this procedure requires a good knowledge of the data and a fair amount of experimentation with the complexity of the model. Another disadvantage is that the parameters of the model are initialized randomly. Thus, the learning process often requires a large training set to find reasonable values of these parameters.

One way of overcoming the problems involved in developing custom models is to use transfer learning, which yields outstanding results for a wide range of applications such as medical image analysis, speech emotion recognition, and quantum phase transition identification [37, 38, 39, 40]. We utilized inductive transfer learning, in which a model originally trained to perform some (unrelated) task is retrained to carry out a new task. The advantage is that the model is already trained to recognize certain patterns. The hope is that the previously learned weights can be fine-tuned to the new task on a relatively small training set. Unfortunately, a negative transfer phenomenon [23] can occur if there are dissimilarities between the original and new task [23, 29]. Indeed we will show that our custom model performs better than transfer learning applied to a VGG16 model originally developed to recognize images of real-world objects.

In this paper, we also use transfer learning ideas to pretrain the model on a large synthetic data set and then apply it to experimental data. This is extremely useful, especially if producing the labeled experimental data is complicated. Pretraining of the models on synthetic data was already successfully used for the tasks of object detection, optical flow estimation, and scene understanding [30, 31, 32]. Before demonstrating the potential of this strategy for our problem we present the precise architecture of the implemented pipeline.

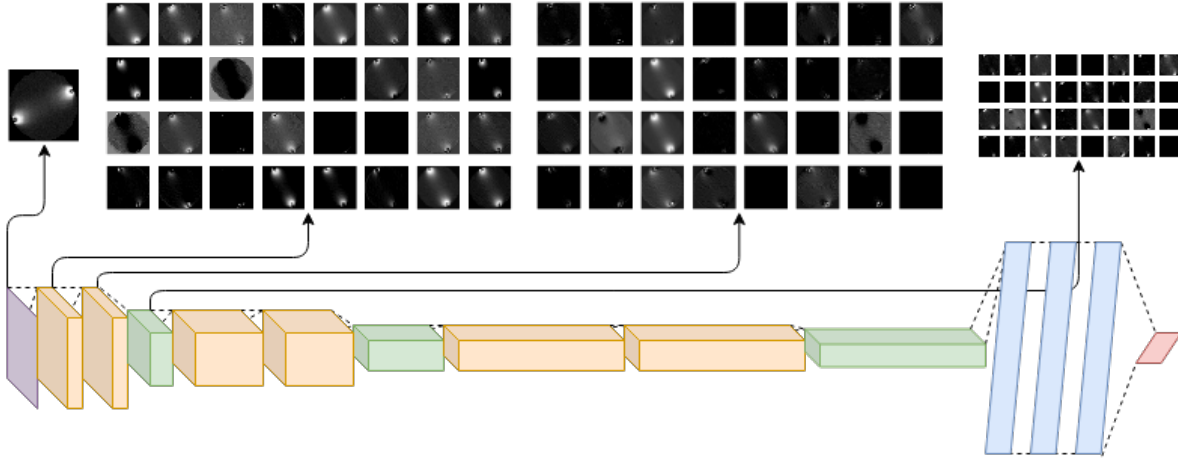


Figure 4. Schematic representation of CNN architecture adopted in our custom model defined in Section 4.2. The input layer is depicted in purple. Convolutional layers are yellow, and pooling layers are green. The fully-connected layers are blue, and the output layer is red. The outputs of the first four layers are shown to indicate how the CNN creates different representations of the image used for the force reconstruction.

4.1. Pipeline Architecture

A single CNN model to reconstruct the forces acting on a particle would have to be rather complex and contain many layers. Therefore, a large training set would be necessary to prevent overfitting. We avoid this problem by dividing the reconstruction of the force list $\{(F_i, \alpha_i, \tau_i)\}_{i=1}^M$ into four smaller units.

The objective of the first unit is to infer the number M . This unit is implemented as a single CNN model. Only after we deduce the number of forces we attempt to reconstruct them. The reconstruction is divided into three additional units: one for inferring the magnitudes F_i , one for the reconstruction of the angles α_i , and finally one for estimating τ_i . As explained in Section 3 the number of forces satisfies $2 \leq M \leq 6$. Thus, each of the additional units is implemented as a collection of five independent CNN models. There is one model for every possible value of M . The choice of the model is based on the output of the first classification unit, responsible for identifying the number of forces.

The general architecture of all the CNN models in individual pipelines is the same. In the case of the pipeline based on our custom model, the choice of the architecture was guided by extensive experiments with different numbers of layers, their dimensions as well as their activation functions. For the transfer learning we utilized the VGG16 model. The following two sections succinctly describe the custom models and models based on VGG16.

4.2. Custom Models

The custom model is inspired by AlexNet [21] and is schematically depicted in Fig. 4. It starts with three pairs of convolutional layers, each followed by a max-pooling layer

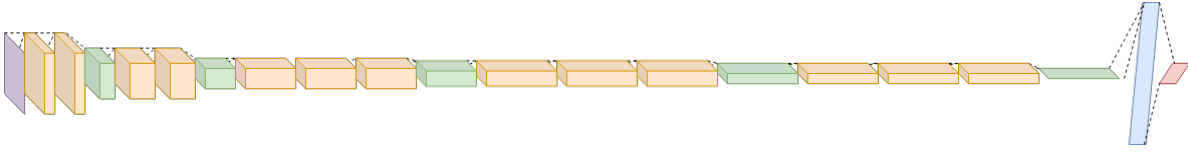


Figure 5. Schematic representation of CNN architecture adopted in the model based on VGG16 defined in Section 4.3. The same color scheme as in Fig 4 is used for the layers.

of size 2×2 pixels. The filters in the convolutional layers are all of the size 3×3 pixels. Each convolutional layer in the first pair has 32 filters, while the layers in the second and third pairs contain 64 and 128 filters respectively. The weights for the layers are initialized using Glorot uniform distribution, which tends to speed up the convergence to the optimal values during the training [41]. For simplicity and computational efficiency, the activation function for convolutional layers is chosen to be ReLu.

To prevent the model from overfitting and to ensure that it only picks up relevant persistent patterns there is a 0.25 dropout regularizer layer after the last pooling layer [42]. The output of this dropout regularizer is flattened to a 1024 dimensional vector that forms an input for a block of three fully connected layers each 1024 wide. The weights of these layers are also initialized using Glorot Uniform distribution and their activation functions are ReLu. The fully connected block is followed by a 0.5 dropout regularizer whose output is processed by the last fully connected layer. The task of this layer depends on the unit. The unit responsible for inferring the number of forces uses the SoftMax activation function for classification purposes [43]. On the other hand, the regression, which is required by units carrying out the reconstruction of the forces, is achieved by a linear activation function [43].

4.3. Models Based on VGG16

For the transfer learning we chose the VGG16 model [22], which won the first place on the ImageNet competition in 2014 with 92.7% test accuracy. While there are models surpassing VGG16 [44, 45, 46], its relative simplicity and low computational cost makes this model well suited for our purpose. The architecture of our model based on VGG16 is depicted in Figure 5.

The VGG16 model was originally trained on 3.9 million images of real-world objects divided into 1,000 distinct classes. Thus, the number and sizes of the convolutional layers are larger than in our custom model. There are two pairs and three triplets of convolutional layers, each followed by a 2×2 pixels pooling layer. Again the filter size is 3×3 pixels for each convolutional layer and their activation functions are ReLu. There are 64 filters in each convolutional layer in the first pair, 128 in the second pair, 256 in the first triplet, and 512 in the rest of the layers.

Since our data set is less complex than the ImageNet, the last four fully connected layers of the original VGG16 model are replaced just by two fully connected layers with a

0.5 dropout layer in-between them. This shrinkage of the fully-connected block is further justified by the input dimensions of our data. Since VGG16 was originally developed for 256×256 image data, in our case, the last convolutional blocks are essentially performing the predictive task of fully-connected layers. The first fully-connected layer in our model has a width 512 and ReLu activation function. The second layer, then, serves as an output layer. Again depending on the task of the unit we either use SoftMax or linear activation function for the output layer.

5. Training of the Neural Networks

The models introduced in the previous section are trained on two particles with different sizes. We first train the models on a particle with radius $r = 1$ and then take these pretrained models and retrain them on a particle with $r = 0.5$ to simulate performance on the experimental data. The data set for the first particle contains 1,024,400 distinct photoelastic patterns accompanied by the force lists that correspond to them. For the second particle, a set of 116,800 images is sufficient because the models have already been pretrained at the time of application.

The resolution of the digital images depicting the patterns is 56 pixels per diameter in both cases. To boost the generalization power of the models we apply Gaussian noise to the images [47, 28]. The noise parameters are based on the intensity field $I(x, y)$ of the pattern. The mean is $0.1 \max_{x,y} I(x, y)$, and the standard deviation is one-tenth of the standard deviation of $I(x, y)$ on the particle. Before discussing the training of different models we first summarize the protocol for generating the data sets used for training purposes.

5.1. Generating of the Data Sets

As explained in Section 2, the photoelastic pattern on a particle can be computed from the list of forces $\{(F_i, \alpha_i, \tau_i)\}_{i=1}^M$ acting on it. To decrease the bias of the model it is important that the force lists in the training set form a representative sample [27]. To ensure that the generated force lists are realistic we enforce the constraints presented in Section 3. We require that forces and torques are balanced and the normal component of the force is larger than its tangential component, i.e. $|\tau_i| \leq \pi/2$. For monodisperse systems, considered in this paper, we get $2 \leq M \leq 6$ and the angles of distinct impact points satisfy $|\alpha_i - \alpha_j| > \pi/3$.

To create a diverse training set with realistic forces we use the following protocol. For each value of M we create the same number of force lists. To construct a force list $\{(F_i, \alpha_i, \tau_i)\}_{i=1}^M$ we start by randomly generating the first $M - 1$ forces. The last force, described by (F_M, α_M, τ_M) , is then added to achieve force and torque balance. The angles

$$\alpha_i \sim \mathcal{U} \left(\frac{2\pi(i-1)}{M} + \frac{\pi}{6}, \frac{2\pi i}{M} - \frac{\pi}{6} \right), \quad 1 \leq i \leq M - 1, \quad (14)$$

are drawn from uniform distributions. The magnitudes of the first $M - 1$ forces are, then, drawn from a normal distribution:

$$F_i \sim \mathcal{N} \left(F, \left(\frac{F}{5} \right)^2 \right), \quad (15)$$

where F is selected from the interval $[0.2, 0.4]$. Finally, each angle τ_i is taken from the normal distribution

$$\tau_i \sim \mathcal{N} \left(0, \frac{\pi}{12} \right). \quad (16)$$

After producing a force list we check that all the magnitudes F_i are positive and $|\tau_i| \leq \pi/2$. If these conditions are not satisfied, then we generate a new force list and discard the old. Finally, it is clear that the above choice of the position angles, α_i , prevents contacts in particular places, which is not desirable. To mitigate this problem we consider between 40 and 80 additional rotations of the particle for each force list constructed above.

5.2. Training the Custom Model Based Pipeline

We recall that our pipeline contains four units. The first classification unit infers the number of forces acting on the particle while the other three regression units reconstruct the individual components of the force list. As suggested in [27] we use the mean absolute error as a loss function for training the regression units. For the classification unit, we utilize a one-hot-encoded vector to describe the probabilities that the object belongs to a particular class and employ the categorical cross-entropy as a loss function.

The stochastic gradient descent with Polyak’s heavy-ball momentum method [48] and a learning rate 10^{-3} is implemented for the optimization process. We experimented with different batch sizes and discovered that a batch size equal to 30 is computationally feasible and has a good regularization effect. We refrain from using the adaptive optimization techniques such as AdaGrad [49] and Adam [50] since they tend to compromise the generalizability of models [51, 52].

To train the individual units we use 80% of the data generated for the particle with radius $r = 1$. The remaining 20% of the data is further equally split into validation and test sets. The classification unit is trained on the whole training set consisting of 829,800 images. As explained in Section 4.1, every regression unit is implemented via five independent CNN models. There is one model for every possible value of M . So, the respective models are only trained on the fifth of the training set with an appropriate number of forces. Finally, the number of epochs is set to 100 which is relatively high. Thus, as suggested in [27], we implement an early stopping criterion which halts the learning process if the error on the validation set does not improve for more than 10 epochs.

5.3. Training the VGG16 Based Pipeline

A similar strategy as for the custom models is used to train the VGG16-based pipeline on the particles with radius $r = 1$. However, instead of allowing all the weights to vary, we fix the weights of the first pair of convolutional layers. This is motivated by the fact that these layers extract general representations (features), which do not need to be adapted [25]. Keeping these layers intact also decreases the chance of overfitting the model. In order to fine-tune the weights, the learning rate is set to 10^{-6} as suggested by the heuristics presented in [25].

Another difference in training the VGG16 based models is that the last fully-connected block is first pretrained on the outputs of the convolutional part of the VGG16 model with the original weights. This warm-up of the last block is important because its weights are initialized randomly. Skipping this step could corrupt the weights of the original VGG16 model, which are supposed to provide useful representations of the data.

5.4. Training on Smaller Particles

To simulate the performance of the models on the experimental data, we retrain the custom model and VGG16-based pipelines on data with particles of size $r = 0.5$. The training procedure for the custom models is exactly the same as before but instead of using random initial weights, we use the weights learned from the particles with radius $r = 1$. In the case of the VGG16 models, the training procedure also stays the same, except that we do not pretrain the last fully-connected layers.

Our goal is to demonstrate that a relatively small data set would be sufficient for retraining the models to perform well on real-world data. To investigate the relation between the accuracy of the force reconstruction and the size of the training set we repeatedly retrain the models, as described above, on the sets of increasing size. In particular, we consider three independent data sets with 1,280, 10,240 and 81,920 samples. As before, every data set contains an equal number of samples for each admissible value of M .

6. Results

In this section, we present our results for reconstructing the forces acting on a particle from its photoelastic response. We start by comparing the performance of our custom model and the transfer learning based on VGG16. As explained in Section 5, both models were trained on a particle with radius $r = 1$ using a synthetic data set with 829,800 training samples and 92,200 validation samples. The presented results were obtained by using a test set of 102,400 images.

The transfer learning approach with VGG16 turns out to identify the number of forces acting on a particle with slightly higher accuracy (0.9998 versus 0.9974) while a more precise force reconstruction is achieved by our custom model. Even though the

Force list component	Mean absolute error of the models	
	Custom model	VGG16 model
Magnitudes [N]	0.00432	0.01125
Impact positions [rad]	0.04488	0.07545
Impact angles [rad]	0.01866	0.05236
	Mean relative error of the models	
Magnitudes	4.206%	11.276%

Table 1. The mean absolute errors of the predicted magnitude, impact position, and impact angle of the forces acting on a particle with radius $r = 1$. The table indicates the errors obtain on a training set with 829,800 samples. For the magnitude, the absolute relative error is provided as well.

number of forces is predicted with high accuracy we investigated possible causes of the misclassification. We realized that most of the particles for which the number of forces is not inferred correctly contain at least one force with a magnitude larger than 0.4N. We recall that we sampled the magnitudes from the distribution $\mathcal{N}\left(F, \left(\frac{F}{5}\right)^2\right)$ where $F \leq 0.4$. Hence, the training set contains only a small number of these particles. If the correct classification at the upper part of the force range is crucial, then we suggest expanding the range slightly to include more particles with relatively extreme forces.

Now we turn our attention to precision of the force reconstruction. To account for the rare misclassifications, discussed above, we first equalized lengths of the force lists by adding an appropriate number of zero triplets to the shorter force list. Then we computed the mean absolute errors for the magnitudes of the forces, their impact positions, and impact angles. In the case of the force magnitudes, we also considered their mean relative error. This error is well defined only if the number of forces acting on a particle is inferred properly. Thus, the mean relative error was evaluated only on the particles for which this number is correctly identified.

Table 1 shows the errors in the prediction of magnitudes of the forces, their impact positions, and impact angles. Note that all the errors are roughly two times smaller for the custom model. Lower accuracy of the transfer learning based on VGG16 models is likely to be caused by the negative transfer phenomenon discussed in Section 4. The high accuracy of our custom model shows that its architecture is well suited for the force reconstruction from photoelastic patterns. In particular, the mean absolute error in prediction of angles describing the impact points of the forces is less than 2.572 degrees. Hence, the absolute error in predicting positions of the impact points is smaller than 1.25 pixels. Despite the high accuracy of the custom model on the synthetic data set, it is not clear how well it would perform on the experimental data. We recall that the images in our data set were intentionally polluted by Gaussian noise as described in Section 5. Thus the force reconstruction seems to be robust with respect to noise. However, there might be further differences between the simulated and experimental data caused for example by errors in measuring the physical parameters of the particles.

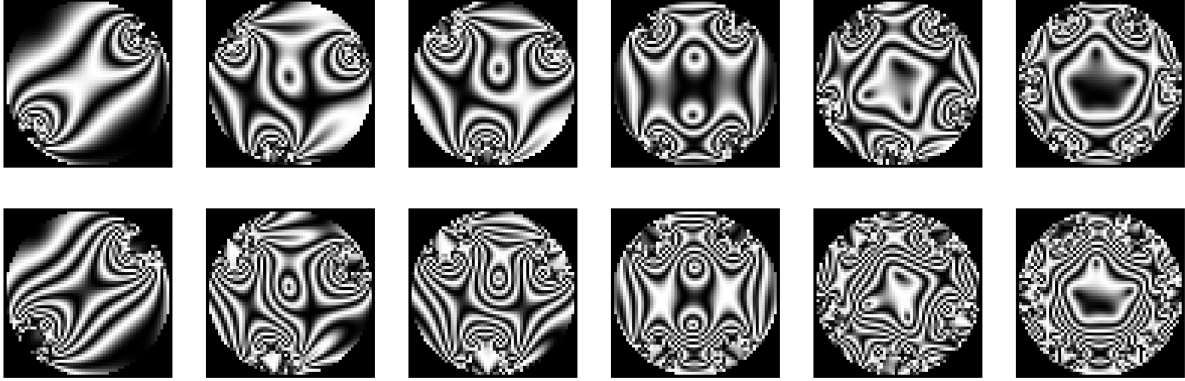


Figure 6. Top row: particles with size $r = 1$. Bottom row: particles with size $r = 0.5$. Particles shown in the same column are subjected to the same forces. Notice the difference in the produced fringe patterns on the surface of the particles.

As we already mentioned, training the models directly on the experimental data is rather unrealistic because the required number of labeled samples is too large. Indeed, the major drawback of using CNNs is that a relatively large training set is necessary to achieve high accuracy. We argue that this problem can be circumvented by pretraining the models on synthetic data. The idea is to first train the models on a large synthetically generated data set and then fine-tune them to the experimental data by using a relatively small data set. Unfortunately, we cannot show the power of this approach directly because we do not have the necessary experimental data. Therefore, we demonstrate its potential by fine-tuning our models to smaller-sized particles, which serve as a proxy for the worst-case difference between the experimental and synthetic data. Figure 6 clearly illustrates that changing the size of the particle dramatically alters the photoelastic response.

Table 2 indicates that reasonable accuracy is already gained by using a training set with 1,280 images. Moreover, similar accuracy as we obtained for the original particle by using 829,800 images is now already achieved on 81,920 training images. As before our custom model outperforms the VGG16 based model suggesting that it is better suited for reconstructing forces acting on a particle from its photoelastic response. Finally, we note that differences between the synthetic and experimental data, shown in [12] are much less severe than the differences caused by our change of the particle size. Therefore, we expect that the sizes of the experimental sets needed to achieve the accuracy levels reported in Table 2 are much smaller.

7. Conclusions

In this paper, we showed the strong potential of using CNNs for reconstructing forces acting between particles in photoelastic granular material. We compared the performance of a custom build model, which we designed, with a transfer learning approach based on VGG16. The better performance and high accuracy of our model

Force list component	Training samples	Mean absolute error of the models	
		Custom model	VGG16 model
Magnitudes [N]	1,280	0.01344	0.02196
	10,240	0.00984	0.01838
	81,920	0.00569	0.01740
Impact positions [rad]	1,280	0.07827	0.11469
	10,240	0.04252	0.10013
	81,920	0.01831	0.07351
Impact angles [rad]	1,280	0.05275	0.08183
	10,240	0.04274	0.09696
	81,920	0.01902	0.09126
		Mean relative error of the models	
Magnitudes	1,280	7.653%	20.549%
	10,240	6.356%	15.651%
	81,920	4.719%	15.335

Table 2. The mean absolute errors of the predicted magnitude, impact position, and impact angle of the forces acting on a particle with radius $r = 0.5$. The table indicates the dependence of the error on the size of the training set. For the magnitude, the absolute relative error is provided as well.

indicate that its architecture is adequate for reconstructing forces acting on a particle from its photoelastic response. However, to achieve the high accuracy of our predictions we had to train the models on a large labeled data set. Unfortunately, it is almost impossible to produce a data set of this size experimentally. Thus, we demonstrated that training on a large experimental data set can be avoided by first pretraining the models on a synthetic data set and then fine-tuning them on a much smaller set produced experimentally.

For simplicity, we only considered monodisperse granular materials. This assumption reduces the number of possible forces acting on an individual particle to six. However, in a particular experiment, the number of forces acting on a particle can be larger and the range of these forces can differ from our choice. In that case our model, available at [53], should be retrained using an appropriate synthetic data set before fine-tuning it to the experimental data. To ensure that the number of forces acting on each particle is detected properly, we suggest using a slightly broader range of forces than the range expected in the experiments.

Finally, to expand our approach to bidisperse materials, used in a variety of experiments [3, 13, 54, 55], an extra module has to be added into the pipeline. So that it contains one module for every particle size. We showed that training the additional module requires a much smaller data set because the original model can be just fine-tuned to the new size of the particle. Finally, using our methods for polydisperse particles or particles with different shapes can be achieved by grouping particles with

similar sizes and shapes together and introducing one module for each group. Naturally, training this pipeline will require larger synthetic data set, as well as more experimental data. However, the current hardware and machine learning software packages make the training feasible on much larger data sets than we used in this paper. Moreover, after the pipeline is trained the force reconstruction becomes extremely fast. Therefore, this approach can be used to analyze the time evolution of granular ensembles consisting of a large number of particles.

Acknowledgment

The authors would like to thank C. Colonnello and L. Kondic for very useful comments on the manuscript. RS was supported by the Undergraduate Research Opportunity Program grant from the University of Oklahoma. MK was supported by a Junior Faculty Fellowship from the University of Oklahoma.

References

- [1] Duran J 2000 *Sands, powders and grains: An introduction to the physics of granular materials* (Springer)
- [2] Bouchaud J, Claudin P, Cates M and Wittmer J 1998 Models of stress propagation in granular media *Physics of dry granular media* (Springer) pp 97–122
- [3] Majmudar T S and Behringer R P 2005 *Nature* **435** 1079
- [4] Clark A H, Petersen A J, Kondic L and Behringer R P 2015 *Physical review letters* **114** 144502
- [5] Falcon E, Castaing B and Creyssels M 2004 *Euro. Phys. J. B* **38** 475–483
- [6] Dorbolo S and Vandewalle N 2002 *Physica A* **311** 307–312
- [7] Jia X, Caroli C and Velicky B 1999 *Phys. Rev. Lett.* **82** 1863
- [8] Makse H A, Gland N, Johnson D J and Schwartz L M 2004 *Phys. Rev. E.* **70** 061302
- [9] Lherminier S, Planet R, Simon G, Vanel L and Ramos O 2014 *Phys. Rev. Lett.* **113** 098001
- [10] Wakabayashi T 1950 *Journal of the Physical Society of Japan* **5** 383–385
- [11] Dantu P 1957 Proceedings of the 4th international conference on soil mechanics and foundations engineering (Butterworths Scientific Publications, London)
- [12] Daniels K E, Kollmer J E and Puckett J G 2017 *Review of Scientific Instruments* **88** 051808
- [13] Wang D, Ren J, Dijksman J A, Zheng H and Behringer R P 2018 *Physical review letters* **120** 208004
- [14] Puckett J Photoelastic disk solver (pediscsolve) <http://nile.physics.ncsu.edu/pub/download/peDiscSolve/>
- [15] Kollmer J Photoelastic grain solver (pegs) <https://github.com/jekollmer/PEGS>.
- [16] Bishop C M 2006 *Pattern Recognition and Machine Learning* (Springer)
- [17] LeCun Y, Bengio Y and Hinton G 2015 *nature* **521** 436–444
- [18] Besacier L, Barnard E, Karpov A and Schultz T 2014 *Speech Communication* **56** 85–100
- [19] Chorowski J and Jaitly N 2016 *arXiv preprint arXiv:1612.02695*
- [20] Jiao L, Zhang F, Liu F, Yang S, Li L, Feng Z and Qu R 2019 *IEEE Access* **7** 128837–128868
- [21] Krizhevsky A, Sutskever I and Hinton G E 2012 Imagenet classification with deep convolutional neural networks *Advances in neural information processing systems* pp 1097–1105
- [22] Simonyan K and Zisserman A 2015 Very deep convolutional networks for large-scale image recognition (Computational and Biological Learning Society) pp 1–14
- [23] Pan S J and Yang Q 2009 *IEEE Transactions on knowledge and data engineering* **22** 1345–1359
- [24] Zhuang F, Qi Z, Duan K, Xi D, Zhu Y, Zhu H, Xiong H and He Q 2020 *Proceedings of the IEEE*

- [25] Yosinski J, Clune J, Bengio Y and Lipson H 2014 How transferable are features in deep neural networks? *Advances in neural information processing systems* pp 3320–3328
- [26] Sharif Razavian A, Azizpour H, Sullivan J and Carlsson S 2014 Cnn features off-the-shelf: an astounding baseline for recognition *Proceedings of the IEEE conference on computer vision and pattern recognition workshops* pp 806–813
- [27] Chollet F 2017 *Deep Learning with Python* (Manning Publications Company) ISBN 9781617294433 URL <https://books.google.com/books?id=Yo3CAQAACAAJ>
- [28] Goodfellow I, Bengio Y, Courville A and Bengio Y 2016 *Deep learning* vol 1 (MIT press Cambridge)
- [29] Kornblith S, Shlens J and Le Q V 2018 *arXiv preprint arXiv:1805.08974*
- [30] Tremblay J, Prakash A, Acuna D, Brophy M, Jampani V, Anil C, To T, Cameracci E, Boochoon S and Birchfield S 2018 Training deep networks with synthetic data: Bridging the reality gap by domain randomization *Proceedings of the IEEE Conference on Computer Vision and Pattern Recognition Workshops* pp 969–977
- [31] Handa A, Patraucean V, Badrinarayanan V, Stent S and Cipolla R 2015 *arXiv preprint arXiv:1511.07041*
- [32] Mayer N, Ilg E, Hausser P, Fischer P, Cremers D, Dosovitskiy A and Brox T 2016 A large dataset to train convolutional networks for disparity, optical flow, and scene flow estimation *Proceedings of the IEEE conference on computer vision and pattern recognition* pp 4040–4048
- [33] Frocht M M 1946 *Photoelasticity* vol 1 (J. Wiley)
- [34] Landau L 1986 *Course of theoretical physics* **7**
- [35] Love A E H 2013 *A treatise on the mathematical theory of elasticity* (Cambridge university press)
- [36] Chau M 2018 *Analyzing 3-point symmetric contacts of photoelastic disks* Ph.D. thesis Reed College
- [37] Shin H C, Roth H R, Gao M, Lu L, Xu Z, Nogues I, Yao J, Mollura D and Summers R M 2016 *IEEE transactions on medical imaging* **35** 1285–1298
- [38] Tajbakhsh N, Shin J Y, Gurudu S R, Hurst R T, Kendall C B, Gotway M B and Liang J 2016 *IEEE transactions on medical imaging* **35** 1299–1312
- [39] Deng J, Zhang Z, Eyben F and Schuller B 2014 *IEEE Signal Processing Letters* **21** 1068–1072
- [40] Huembeli P, Dauphin A and Wittek P 2018 *Physical Review B* **97** 134109
- [41] Glorot X and Bengio Y 2010 Understanding the difficulty of training deep feedforward neural networks *Proceedings of the thirteenth international conference on artificial intelligence and statistics* pp 249–256
- [42] Srivastava N, Hinton G, Krizhevsky A, Sutskever I and Salakhutdinov R 2014 *The journal of machine learning research* **15** 1929–1958
- [43] Goodfellow I, Bengio Y and Courville A 2016 6.2. 2.3 softmax units for multinoulli output distributions *Deep Learning*. (MIT Press) pp 180–184
- [44] Chollet F 2017 Xception: Deep learning with depthwise separable convolutions *Proceedings of the IEEE conference on computer vision and pattern recognition* pp 1251–1258
- [45] Szegedy C, Ioffe S, Vanhoucke V and Alemi A 2016 *arXiv preprint arXiv:1602.07261*
- [46] Xie S, Girshick R, Dollár P, Tu Z and He K 2017 Aggregated residual transformations for deep neural networks *Proceedings of the IEEE conference on computer vision and pattern recognition* pp 1492–1500
- [47] Bishop C M 1995 *Neural computation* **7** 108–116
- [48] Polyak B T 1964 *USSR Computational Mathematics and Mathematical Physics* **4** 1–17
- [49] Hadgu A T, Nigam A and Diaz-Aviles E 2015 Large-scale learning with adagrad on spark 2015 *IEEE International Conference on Big Data (Big Data)* (IEEE) pp 2828–2830
- [50] Chilimbi T, Suzue Y, Apacible J and Kalyanaraman K 2014 Project adam: Building an efficient and scalable deep learning training system *11th {USENIX} Symposium on Operating Systems Design and Implementation ({OSDI} 14)* pp 571–582
- [51] Wilson A C, Roelofs R, Stern M, Srebro N and Recht B 2017 The marginal value of adaptive gradient methods in machine learning *Advances in neural information processing systems* pp 4148–4158

- [52] Zhang Z 2018 Improved adam optimizer for deep neural networks *2018 IEEE/ACM 26th International Symposium on Quality of Service (IWQoS)* (IEEE) pp 1–2
- [53] Sergazinov R and Kramár M 2020 Convolutional neural networks for force reconstruction in granular media <https://github.com/mrsergazinov/PhotoForceReconML>
- [54] Dijkstra J A, Kovalcinova L, Ren J, Behringer R P, Kramár M, Mischaikow K and Kondic L 2018 *Physical Review E* **97** 042903
- [55] Tordesillas A, Walker D M, Froyland G, Zhang J and Behringer R P 2012 *Physical Review E* **86** 011306